Volume 51
Number 32
28 August 2022
Pages 11939-12390

Dalton Transactions

An international journal of inorganic chemistry

rsc.li/dalton

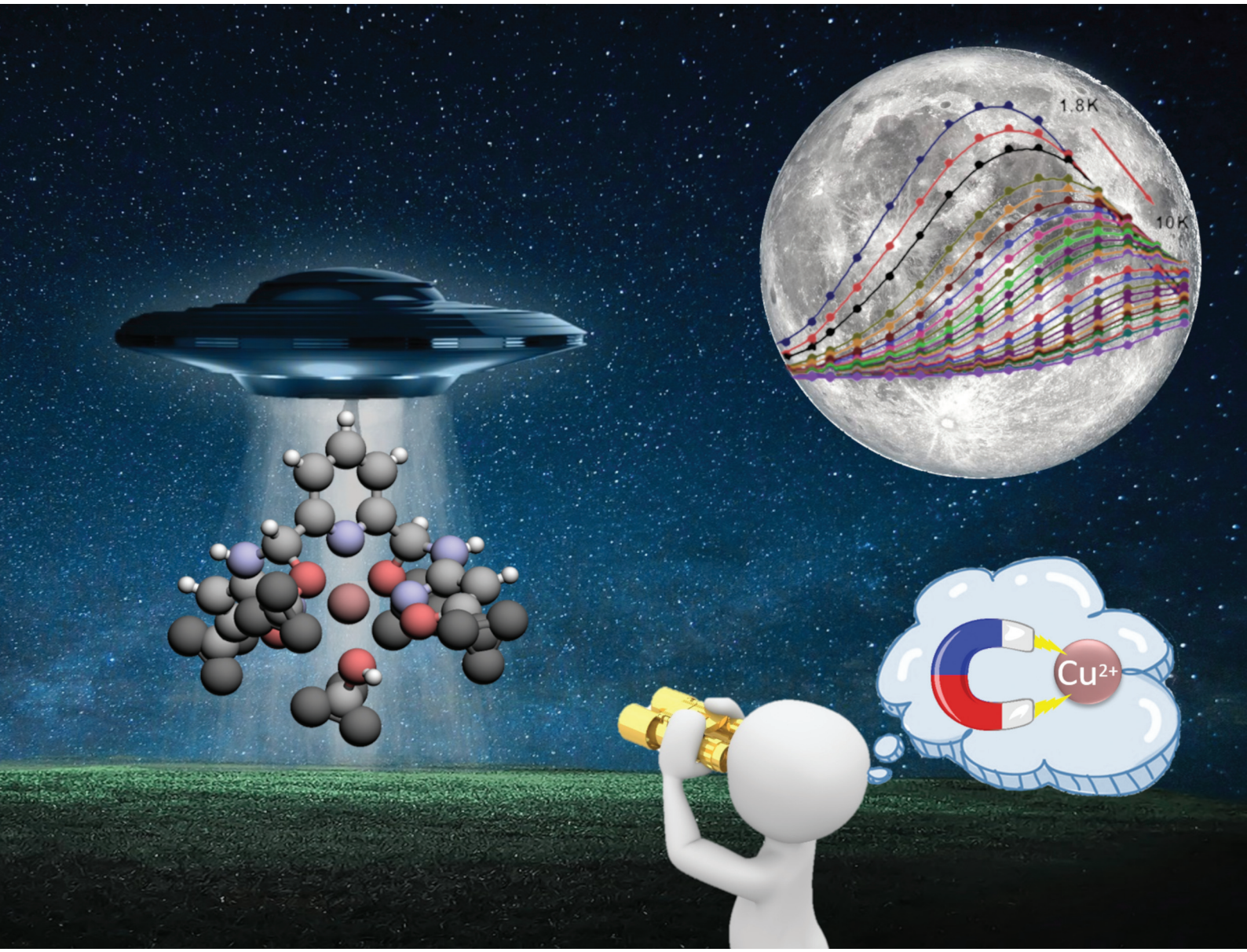

ISSN 1477-9226

ROYAL SOCIETY OF CHEMISTRY

PAPER

Adam Gorczyński, Maria Korabik *et al.*
Understanding the effect of structural changes on slow magnetic relaxation in mononuclear octahedral copper(II) complexes

Dalton Transactions

ROYAL SOCIETY OF CHEMISTRY

PAPER

View Article Online
View Journal | View Issue

Cite this: *Dalton Trans.*, 2022, **51**, 12041

Understanding the effect of structural changes on slow magnetic relaxation in mononuclear octahedral copper(II) complexes†

Dawid Marcinkowski, ‡[a] Ariel Adamski,‡[a] Maciej Kubicki, [a] Giuseppe Consiglio,[b] Violetta Patroniak, [a] Tomasz Ślusarski,[a,c] Muhammed Açıkgöz,[d] Daria Szeliga,[e] Nahir Vadra, [a,f] Mirosław Karbowiak, [e] Ireneusz Stefaniuk,[g] Czesław Rudowicz, [a] Adam Gorczyński [a]* and Maria Korabik*[e]

Current advances in molecular magnetism are aimed at the construction of molecular nanomagnets and spin qubits for their utilization as high-density data storage materials and quantum computers. Mononuclear coordination compounds with low spin values of $S = \frac{1}{2}$ are excellent candidates for this endeavour, but knowledge of their construction *via* rational design is limited. This particularly applies to the single copper(II) spin center, having been only recently demonstrated to exhibit slow relaxation of magnetisation in the appropriate octahedral environment. We have thus prepared a unique organic scaffold that would allow one to gain in-depth insight into how purposeful structural differences affect the slow magnetic relaxation in monometallic, transition metal complexes. As a proof-of-principle, we demonstrate how one can construct two, structurally very similar complexes with isolated Cu(II) ions in an octahedral ligand environment, the magnetic properties of which differ significantly. The differences in structural symmetry effects and in magnetic relaxation are corroborated with a series of experimental techniques and theoretical approaches, showing how symmetry distortions and crystal packing affect the relaxation behaviour in these isolated Cu(II) systems. Our unique organic platform can be efficiently utilized for the construction of various transition-metal ion systems in the future, effectively providing a model system for investigation of magnetic relaxation *via* targeted structural distortions.

Received 19th May 2022,
Accepted 21st June 2022

DOI: 10.1039/d2dt01564a

rsc.li/dalton

1. Introduction

Molecular nanomagnets (MNMs) are a research focus of scientists due to a variety of potential applications,[1–4] including molecular spintronics,[1,5,6] high-density information storage,[7–9] quantum information processing or sensing.[10–16] These systems display magnetic hysteresis below their blocking temperature (T_B) and are magnetically bi-stable, exhibiting an energy barrier to spin reversal (U_{eff}),[17–22] ultimately manifested by macroscopic quantum tunneling of magnetization (QTM) and slow relaxation of magnetization. The discovery of the highest T_B by Guo *et al.*,[23] for an organometallic Dy(III) complex displaying magnetic hysteresis at temperatures reaching 80 K, could facilitate development of high-temperature SIM devices. In addition, studies of various Dy(III) congeners of this family[24–26] indicate the importance of understanding the magnetization relaxation mechanisms and magneto-structural correlations.[4,27–33] Still, similar level of performance for d-block MNMs is yet to be achieved.

Prerequisites for utilization of 3d complexes as molecular nanomagnets are well-established.[3,34] Importantly, the $S = \frac{1}{2}$

[a]*Faculty of Chemistry, Adam Mickiewicz University, Uniwersytetu Poznańskiego 8, 61-614 Poznań, Poland. E-mail: adam.gorczynski@amu.edu.pl*
[b]*Dipartimento di Scienze Chimiche, Università di Catania, I-95125 Catania, Italy*
[c]*Institute of Spintronics and Quantum Information, Faculty of Physics, Adam Mickiewicz University, Uniwersytetu Poznańskiego 2, 61-614 Poznań, Poland*
[d]*Department of Science, The State University of New York (SUNY) Maritime College, New York 10465, USA*
[e]*Faculty of Chemistry, University of Wrocław, F. Joliot-Curie 14, 50-383 Wrocław, Poland. E-mail: maria.korabik@chem.uni.wroc.pl*
[f]*Universidad de Buenos Aires, Facultad de Ciencias Exactas y Naturales, Departamento de Química Inorgánica, Analítica y Química Física and CONICET – Universidad de Buenos Aires, Instituto de Química Física de los Materiales, Medio Ambiente y Energía (INQUIMAE), Buenos Aires C1428EGA, Argentina*
[g]*College of Natural Sciences, University of Rzeszow, Rejtana 16a, 35-310 Rzeszow, Poland*

†Electronic supplementary information (ESI) available: Experimental synthetic details, part of magnetic, spectroscopic and theoretical details. CCDC 1965451, 1965452 and 2150965. For ESI and crystallographic data in CIF or other electronic format see DOI: https://doi.org/10.1039/d2dt01564a

‡Dawid Marcinkowski and Ariel Adamski contributed equally.

systems are excellent candidates for construction of molecular qubits.[35,36] Chosen examples based on V(IV),[37–41] Fe(V),[42,43] Mn (IV),[44] Ni(III)[45] or Ni(I)[46,47] metal ions show how the choice of ligand, electronic configuration of the metal ion and the observed symmetry distortions all affect the magnetic relaxation and its mechanisms, which include combined phonon, direct and Raman processes.[48,49] The above compounds are important contributions, nonetheless they are usually pretty unstable at room temperature, which would limit their potential applications. Copper(II) ion on the other hand forms very stable complexes and was demonstrated to be of interest for molecular magnetism studies. Notable examples of $S = \frac{1}{2}$, d^9 Cu(II) systems were proposed to act as potential spin qubits with phthalocyanines,[50,51] porphyrines[52–55] acetylacetonates or dithiocatecholates ligating species.[56–58] Recent record value of 1.4 ms coherence time was demonstrated by Dai *et al.*[56] for a $(PPh_4)_2[Cu(mnt)_2]$ (where mnt^{2-} is maleonitriledithiolate), after dilution in isostructural diamagnetic Ni(II) matrix and utilization of dynamic decoupling technique. As for the SIM behavior, the examples of compounds with experimentally determined field-induced slow magnetic relaxation with single d^9 Cu(II) ion are rather scarce,[59–64] whereas its origin is only partially understood.[48,49]

To achieve the desired molecular magnetic behavior in $S = \frac{1}{2}$ coordination systems, the following molecular design were proposed: (i) square planar coordination geometry; (ii) coordinating atoms devoid of nuclear spin; (iii) rigidification of the molecular architecture; (iv) minimization of the protons influence above a certain radius from the metal (the concept of spin diffusion barrier).[14,54,65,66] Nevertheless, yet undiscovered features may also be important, which can be established through meticulous magneto-structural correlation studies. These can be facilitated by employing modular organic platforms, since they may provide possible predictions of magnetic parameters based on the structure alone.[48]

Herein, we present a unique example of system, which is suitable for construction of monometallic transition metal complexes, the structure of which can be carefully altered within the ascertained symmetry regime. Stereospecific addition of alcohol to imine ligand leads to pentadentate ligands, which readily coordinate Cu(II) ion to form octahedral complexes (Scheme 1).

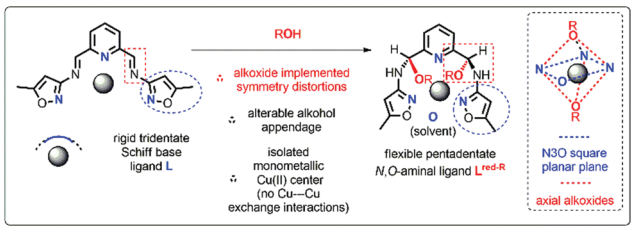

Scheme 1 Rationale behind the modular organic platform designed and implemented in the present studies for monometallic magneto-structural correlations.

This framework is close to the N_3O square plane, whereas symmetry distortions are then applied through the axial alkoxide moieties. Alterable alcohol appendage and single Cu(II) ionic centre with blocked intermetallic exchange interactions make this platform a suitable starting point for better understanding of relaxation mechanisms and establishing magneto-structural correlations. The effect of the surrounding ligands and symmetry of the polyhedron on the static and dynamic magnetic properties of Cu(II) ions in two systems is investigated. To rationalize our experimental results extensive computational studies are carried out utilizing SHAPE analysis, density functional theory (DFT)/*ab initio* and semiempirical approaches. This combined strategy enables to draw conclusions on magnetization relaxation mechanisms, magneto-structural correlations, the role of structural distortions, and usefulness of the proposed organic platform for designing new Cu(II) SIMs/qubits.

2. Results and discussion

2.1 Synthesis

Schiff base ligand **L** was synthesized *via* condensation of 2,6-pyridinedicarboxaldehyde with 3-amino-5-methylisoxazole as presented in Scheme 2. Although **L** was isolated and characterized (see Section II in ESI†), its complexation with CuX_2 salts in the presence of alcohols leads to unexpected structural transformations. Reactions of **L** with $Cu(ClO_4)_2{\cdot}6H_2O$ (**1**) and $Cu(OTf)_2$ (**2**) lead to the asymmetric addition of MeOH (**1**) or EtOH (**2**) to the imine bond, resulting in the formation of chiral *N*,*O*-aminal $\mathbf{L}^{\mathbf{red\text{-}1/2}}$, which is unambiguously established *via* X-ray crystallography of isolated coordination compounds **1** and **2** (Table S1† and Section 2.2). Whereas reduction of the parent ligand **L** is most plausibly facilitated by the template effect of Cu(II) ions, it is yet to be determined if such reaction is diastereospecific or one of the chiral isomers (here *S*,*S*) crystallized in the preferential manner. The solvent as well as the counter ions OTf^- and ClO_4^- does not seem to affect the type of the isomer obtained in both structures. Such chiral *N*,*O*-aminal motif is found in a number of natural, pharmaceutical products and valuable synthetic precursors.[67–69] Therefore, the development of effective and effortless methods for their synthesis has attracted considerable research effort.[70,71] This report is the first on the formation of aldimine-derived *N*,*O*-aminals, without the need of applying the external chiral catalyst. Interestingly, only three studies[70,72,73] on the use of metal-

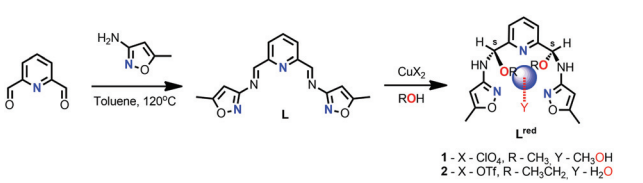

Scheme 2 Synthetic pathway leading to Schiff base ligand **L** and its copper(II) complexes; blue sphere represents Cu(II) ion.

lic catalysts in the formation of *N*,*O*-aminals from related ketimines were reported so far. Altogether, our approach can be used to form chiral molecules with the *N*,*O*-aminals, strategically placed at the 2,6-positions of pyridine, for potential use in construction of more complex systems, particularly of biological or magnetic relevance.

2.2 Structural characterization of Cu(II) complexes

Fig. 1a and b shows the perspective views of molecules **1** (a) and **2** (b) together with the numbering schemes. Table S2† lists the relevant geometrical parameters. Structures were refined for the perchlorate analogue at room- (**1**) and liquid nitrogen-temperature (**1′**) to unambiguously exclude phase-transition changes. Pentadentate ligands $\mathbf{L_{red}}^{1}$ (ClO_4^-; MeOH) and $\mathbf{L_{red}}^{2}$ (OTf–, EtOH) wrap around copper(II) ions and differ by either methoxy (**1**) or ethoxy (**2**) groups attached to the stereogenic center, as a result of the unexpected addition of alcohol to the imine bond (Scheme 2).

In both crystal structures complexes exist as dications, with two perchlorate (**1**) or triflate (**2**) anions balancing the charge. Cu(II) centers are six-coordinated in distorted octahedral fashion (Fig. 1c). Due to the structure of the ligand the octahedra are elongated along one direction (O7···O14), and this elongation is as large as 25% in **1** and slightly smaller in **2** (Fig. 1c and d). Such a geometry is related to the conformation of ligand molecules, in which the ring planes are almost perpendicular one to another (Table S2†). This also results in a nearly square tetradentate plane formed by three nitrogen atoms of the $\mathbf{L^{red\text{-}1/2}}$ ligand and the oxygen atom from the solvent molecule (see SHAPE analysis in Section 2.3). Both compounds crystallize in the triclinic crystal system and $P\bar{1}$ space group, with two molecules of Cu(II) complex in a unit cell. In the crystal structure of **1**, they symmetrically interact with each other through the pyridine–pyridine π–π stacking interactions (C_2 relation, smallest Cu···Cu distance *ca*. 8 Å). These form infinite chains of alternate cations and anions connected by the hydrogen bonds, with the second anion threaded to this chain (Fig. 1f and Table S3†). In **2**, the main structural motif is a cluster of hydrogen bonded structural fragments: two cations (C_2 relation, smallest Cu···Cu distance *ca*. 9.7 Å), four triflate anions, and two solvent-ethanol molecules (Fig. 1g). These principal motifs are connected to form three-dimensional crystal structure by means of electrostatic interactions and weak intermolecular van der Waals forces, thus lacking of the degree of organization present in **1**.

2.3 SHAPE analysis and symmetry considerations

To gain more insight into the local site-symmetry in **1** and **2**, calculations using SHAPE software[74,75] were performed, which utilize the continuous shape measurements (CShM)[76] method. *S* parameter is therefore introduced, which corresponds to the degree of deviations from the perfect polyhedron with $S = 0$ corresponding to ideal geometry. Results shown in Table S4† clearly indicate that **1** and **2**, as well as magnetically relevant Cu(II) system studied by Boča[60] show significant deviations from the octahedral geometry, classified as structurally severe distortions ($S > 3$).[74] Please note that the chemically significant differences were classified to be visible from 0.1 value changes.[74]

Given that investigated systems are heterotopic in terms of ligands nature (N and O donor atoms), we performed additional analysis regarding square planar planes present in the studied octahedra. The aim was to understand: (i) which part of the ligands architecture is responsible for structural anisotropy of relevance to magnetic properties and (ii) why do the observed magnetic properties differ in **1** and **2**. Results are gathered in Table S5.† One can discriminate three planes: (*A*) (N2–N9–N17–MeOH/H_2O) which is dependent on the monodentate MeOH (**1**) or H_2O (**2**) solvent molecules; (*B*) (MeOH/H_2O–N9–O7–O14) and (*C*) (N2–N17–O7–O14) which are mostly affected by the O7–O14, distortions. Unexpectedly, it appears that plane (*A*) alone exhibits significantly larger distortions in

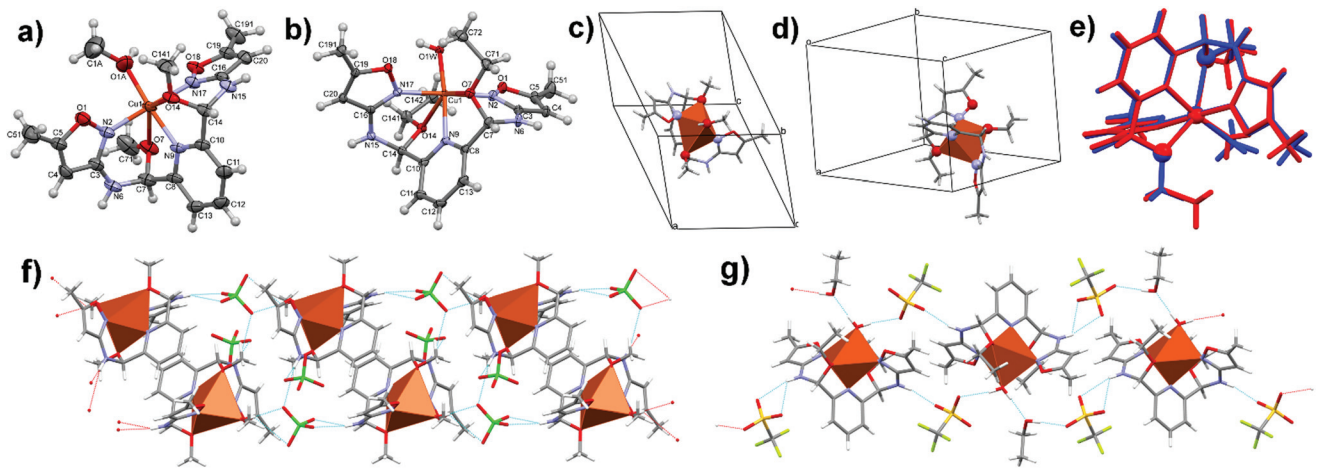

Fig. 1 Perspective views of dicationic complexes **1** (a) and **2** (b). Ellipsoids are drawn at the 50% probability level, hydrogen atoms are shown as spheres of arbitrary units; the orientations of long axis of the coordination octahedron in **1** (c) and **2** (d); (e) superimposed structures of dicationic complexes **1** (blue) and **2** (red); crystal lattice packing and hydrogen-bond motifs in **1** (f) and **2** (g); hydrogen bonds are shown as blue dashed lines.

complex **2** (*S*-value **2** = 0.308 *vs.* *S*-value **1** = 0.077). This could be also dependent on the H-bonding pattern with the perchlorate (**1**) or triflate (**2**) counterions. *S*-Values in planes (*B*) and (*C*) favour stronger distortions in **1** than in **2**, ascribed to the plane formed by isoxazole/alkoxide moieties.

2.4 DC magnetic properties

The magnetic properties of powdered microcrystalline samples **1** and **2** were studied by measuring the thermal dependence of the magnetic susceptibility in the temperature range of 1.8–300 K and magnetic field of 0.5 T. The field dependences of the magnetization from 0 to 5 T for **1** and **2** were measured at 2 K. In DC magnetic field both compounds show similar properties, typical for non-interacting $S = \frac{1}{2}$ spin system (Fig. S2†). The $\chi_m T$ product values (0.373 ± 0.005 cm^3 K mol^{-1}, μ_{eff} = 1.73 ± 0.01 B.M.) are practically constant in the whole measured temperature range 1.8–300 K. The $1/\chi_m$ *versus* *T* plots obeys the Curie–Weiss law with Curie constant *C* = 0.384 and 0.393 cm^3 K mol^{-1} and Weiss constant $\theta = -0.1$ and −0.3 K for **1** and **2**, respectively. Simulation of magnetic susceptibility curves using molecular field correction:[77,78]

$$\chi_m = \frac{\chi}{\left(\frac{2zJ'}{Ng^2\beta^2}\right)\chi} \quad (1)$$

incorporated in the PHI program[79] yields very low parameters: $zJ' = -0.05$ and -0.10 cm^{-1} for **1** and **2**, respectively. The goodness of agreement factor *R*, defined as:

$$R = \sum_{i=1}^{n} \frac{(\chi_i^{exp}T - \chi_i^{calc}T)^2}{(\chi_i^{exp}T)^2} \quad (2)$$

was obtained as: $R = 4.43 \times 10^{-6}$ and 2.02×10^{-6} for **1** and **2**, respectively. This finding confirms that Cu(II) centers are practically magnetically isolated in both compounds, in accordance with determined X-ray structures (see Section 2.2). Hence the effect of exchange interactions between Cu(II) ions may be excluded. Magnetically isolated Cu(II) ions in the crystal structure of **1** and **2** are also confirmed by magnetization *versus* field measurements measured at 2 K (Fig. S3†). Experimental points agree with the Brillouin function for $S = \frac{1}{2}$ and $g = 2$.

2.5 AC magnetic properties

Measurements were made at 3×10^{-4} T oscillating field for 16 frequencies, in the temperature range 1.8–10 K. An external magnetic DC field of 0.1 T was chosen from the maximum of out of phase susceptibility χ'' *versus* magnetic field relation (Fig. S4 and S5†). Please notice that much stronger field must be applied for complex **2** than for **1**, which also correlates with more pronounced character of slow magnetic relaxation in AC field for the latter one (*vide infra*). The out of phase component χ'' of **1** and **2** is silent at zero DC field, which indicates that the magnetization relaxation time (τ) is much shorter than $\frac{1}{2}\pi\nu$ of the AC field. Measurements done under 0.1 T DC field reveal differences in properties of complexes **1** and **2**. The in-phase χ' (Fig. 2a) and out-of-phase χ'' (Fig. 2b and c) susceptibilities show temperature and frequency dependence with characteristic maxima in **1**, indicating slow magnetic relaxation phenomenon. Different types of relaxation mechanisms can be potentially involved in molecular system: Orbach, direct, Raman, and QTM components, respectively.[60,61]

$$\tau^{-1} = {\tau_0}^{-1} \exp\left(-\frac{U}{k_B T}\right) + aT + bT^n + {\tau_{QTM}}^{-1} \quad (3)$$

In the literature, one can find different approaches to the Arrhenius equation:

$$\tau^{-1} = {\tau_0}^{-1} \exp\left(-\frac{U}{k_B T}\right) \quad (4)$$

performed in AC magnetic field studies for the relaxation processes observed for coordination compounds with spin $S = \frac{1}{2}$. Some authors suggest that τ does not follow the Arrhenius behavior, because of lack of magnetic states besides $m_S = \pm\frac{1}{2}$ doublet that can be thermally populated providing a path for the multiphonon Orbach mechanism of relaxation. Consequently, they propose to use Raman and direct mechanisms, which dominate at high and low temperature respectively.[35,37,39] Other authors, such as Boca *et al.*,[60] use Arrhenius-like plot to determine activation energy of the relaxation process U/k_B and τ_0, admitting that effective energy barrier due to the zero-field splitting (ZFS) of the ground term does not exist in the Cu(II) system. It results in elimination of the Orbach mechanism in relaxation process in $S = \frac{1}{2}$ com-

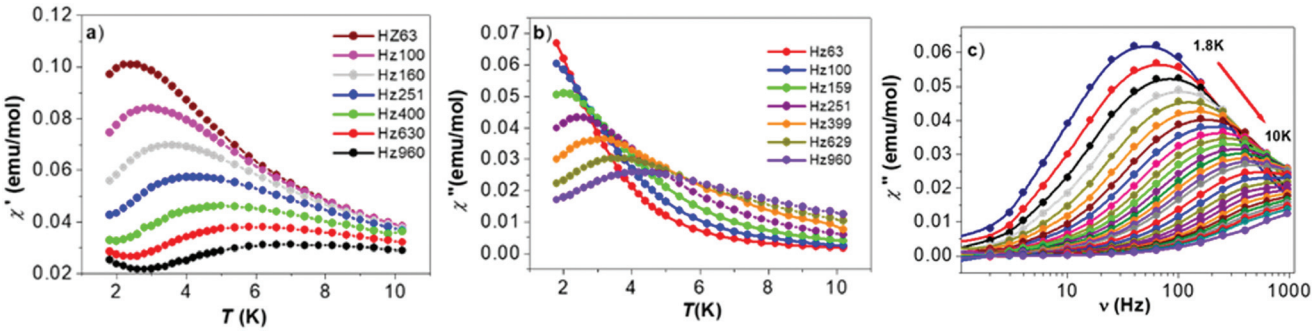

Fig. 2 Temperature dependence of: (a) the in-phase χ', (b) the out-of-phase χ'' susceptibility and (c) χ'' *vs.* frequency for complex **1**.

pounds. In the Raman process, relaxation follows through a virtual state. The direct process describes relaxation from $-\frac{1}{2}$ to $+\frac{1}{2}$ states with emission of a single lattice phonon. Relaxation through QTM is facilitated by the systems transverse anisotropy.[60,64]

The analysis of the relaxation processes in **1** was carried out using Raman, direct and QTM relaxation mechanisms. The fact that Raman mechanism plays a dominant role in $S = \frac{1}{2}$ system[37] and that the $\ln \tau$ *vs.* $\ln T$ dependence is almost linear (Fig. S6†), suggests that direct relaxation mechanism cannot be ignored.[37] A linear fit to the equation $\ln \tau = b_0 + b_1 \ln T$ was used to determine direct process parameters, which are $b_0 = -4.50$ and $b_1 = -2.07$ and they are comparable to that recently obtained for Cu(II) $S = 1/2$ system.[20] We have also attempted to extract the direct process term from field dependence of τ^{-1}.

The direct spin relaxation mechanism can be expressed by the following equation:[80,81]

$$\tau^{-1} = AH^4T \quad (5)$$

where A is an adjustable parameter, H is the external DC field, T is the temperature. The value of H(DC) = 0.1 T was used to determine the value of A for the direct mechanism and 1649 s^{-1} T^{-4} K^{-1} was obtained. The fitting results are shown in Table 1 and Fig. 3a. Calculations taking into account Raman, direct, and QTM mechanisms gave the respective parameters as: $b = 18.59$ s^{-1} $K^{-1.32}$, $n = 1.32$; $a = 1.06$ and QTM equal 0.29. These values are similar to those found for $S = \frac{1}{2}$ spins in Cu(II) complexes.[61] It is worth to note that all relaxation parameters obtained by us are comparable with those published by Cui *et al.*[61] for five coordinate Cu(II) complex.

The Cole–Cole plots from the AC magnetic susceptibility data of **1** (Fig. 3b) were fitted by the generalized Debye model (Table S6†).[82,83] The α parameters describing the distribution of the relaxation times in a magnetic system were extracted. The limiting value of $\alpha = 0$ describes a single relaxation process, whereas $\alpha = 1$ corresponds to an infinitely wide distribution of the relaxation times. The wider the distribution of the relaxation times, the larger the value of α.[82] A small value of the distribution coefficient α (0.16 at 4.4 K to 0.25 at 1.8 K) for complex **1** indicates that the relaxation process has a narrow distribution of relaxation time. The τ parameters were extracted from the Debye model (Fig. S6†), with $\tau = 3.97$ ms at 1.8.K. Similar temperature relations and values were presented for vanadium(IV)-based compounds, with $S = \frac{1}{2}$.[38]

AC susceptibility measurements of complex **2** differ from **1**, with no phase shift maxima present in the in-phase χ' *vs.* T dependencies (Fig. 4a) and only the slight onset of the out-of-phase signals χ'' *vs.* T (Fig. 4b and c) under high external magnetic field frequencies. Despite high structural resemblance of the Cu(II) coordination environment, the properties of **1** and **2** differ significantly and this precluded us from determination of the relaxation parameters for the latter compound.

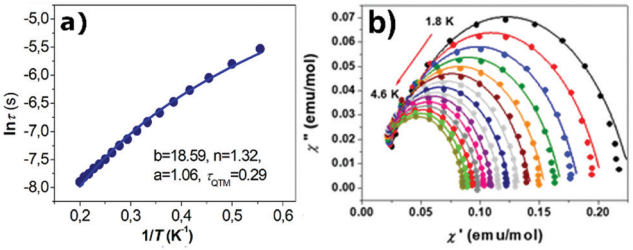

Fig. 3 (a) Magnetization relaxation time ln(τ) in a function of reciprocal temperature T^{-1} of **1**. The effect of using Raman + direct + QTM in fitting procedure is presented in the form of a continuous line; (b) Cole–Cole plots for **1** under 0.15 T DC field. The solid lines are the best fits to the experiments with the generalized Debye model.

2.6 CW-EPR

Continuous wave electron paramagnetic resonance (CW-EPR) spectra were recorded in X and Q band frequencies to corroborate magnetic phenomena (Sections 2.4 and 2.5) with structural studies (Sections 2.2 and 2.3). For experimental details see EPR Section III in the ESI.† CW-EPR spectra of complexes **1** and **2** in liquid nitrogen (X-band) and helium (Q-band) temperatures with fitting protocols are shown in the ESI (Fig. S7–S16†) with representative ones in Fig. 5. The spectroscopic splitting factors $g_\perp$ and $g_\parallel$ for all spectra are presented in Table 2 and prove their axial character type ($g_\parallel > g_\perp$). Transition energy levels at the resonance field B_{res} are presented in Tables S7 and S8† and their graphical representation in Fig. S17 and S18.† Room temperature X-band EPR spectra of **1** and **2** (Fig. 5a and b) are temperature-independent down to 77 K. For **1** the axial type spectrum is partially, but clearly resolved with the g-factors $g_\perp = 2.06$, $g_\parallel = 2.28$ and parallel hyperfine splitting parameter $A_\parallel = 175$ G, resulting from the interaction of the unpaired electron of Cu(II) with the spin of copper nucleus $I = 3/2$. It is identical for both natural isotopes of ^{63}Cu and ^{65}Cu, so eight hyperfine levels can be expected with four allowed transitions: $\Delta M_S = \pm 1$ and $\Delta M_I = 0$ (Fig. S19†).[84] The axial EPR spectrum of complex **2** exhibits similar values of the g-factors: $g_\perp = 2.06$ and $g_\parallel = 2.25$ but with no hyperfine structure.

Table 1 Fitting of different relaxation parameters of complex **1** determined from AC studies based on Fig. 3a

Relaxation mechanism: Raman + direct + QTM	a (s^{-1} K^{-1})	A^a (s^{-1} T^{-4} K^{-1})	b (s^{-1} K^n)	n	τ_{QTM}, s^{-1}	Ref.
DC field 0.15 T	0.93	1838.51(9)	8.31(3)	3.10(2)	0.02	61
DC field 0.10 T	1.06(2)	1649.32(1)	18.59(2)	1.32(1)	0.29(2)	This work

[a] Calculated from field dependence of τ^{-1}.

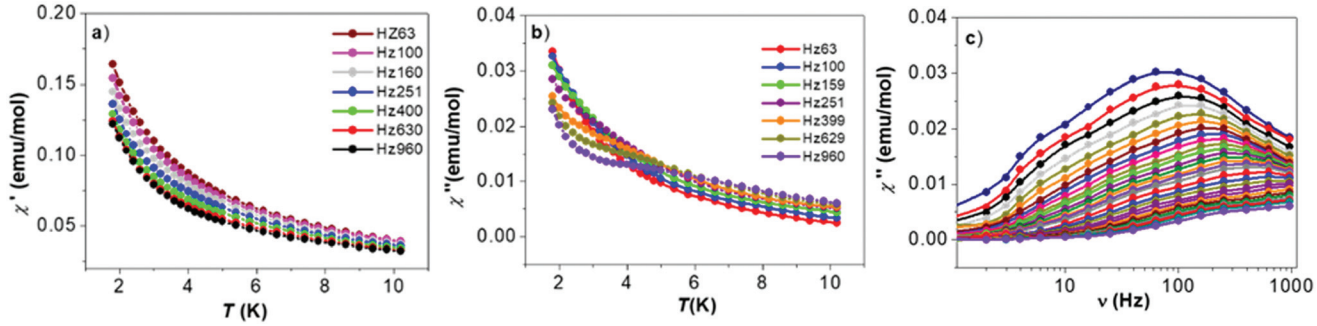

Fig. 4 Temperature dependence of: (a) the in-phase χ', (b) the out-of-phase χ'' susceptibility and (c) χ'' *vs.* frequency dependence of the complex **2**.

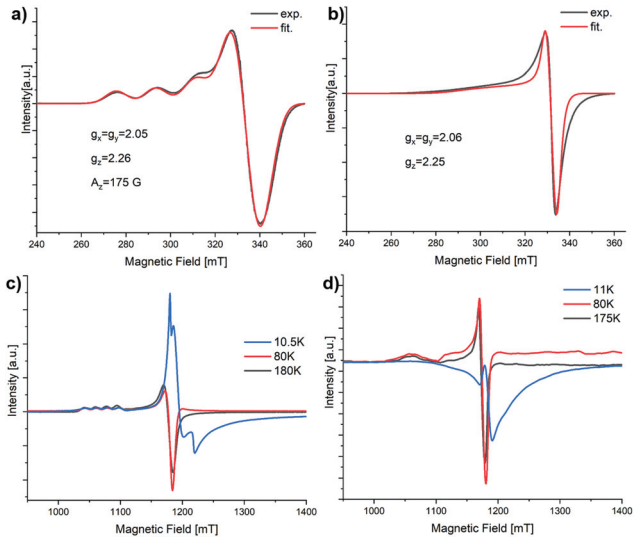

Fig. 5 X-band EPR spectra of **1** (a) and **2** (b) at RT; solid red line shows temperature independent simulated spectra with parameters presented. The same type of spectrum with the same parameters was observed at 77 K; superposition of Q-band spectra of **1** (c) and 2 (d) at chosen temperature intervals: simulated spectra are in the ESI.†

From spectra in Q-band (Fig. 5c and d) valuable information can be obtained, because the hyperfine structures are more pronounced for both compounds and it can be also observed for complex **2**, which was not the case for X-band frequencies.

Down in helium temperatures, formation of a bimodal peak is observed for complex **1** in the range of 1200–1300 mT magnetic field. The second line is an image of transitions in the perpendicular direction (*i.e.* $xy \| B$), this effect is clearly observed for sample **1**, while for sample **2** it is less apparent due to larger line widths. This phenomenon is even more visible in temperature-dependent EPR spectra (Fig. S7 and S8†). In addition, the LFMA (low field microwave absorption) line, which is an indicator of ferromagnetic interactions, does not occur even up to helium temperatures for both tested samples. This means ferromagnetic interactions are not present in **1** and **2**, which is consistent with the DC susceptibility studies (see Section 2.4). While the nature of this phenomenon is yet to be unambiguously established, purity of synthesized samples and the fact that it is manifested in both compounds **1** and **2** (although to a different extent, *i.e.* sharp

Table 2 The fitted SH parameters: Zeeman factors (g_i; dimensionless), hyperfine interaction (A_i; in 10^{-4} cm^{-1}) and spectral parameters for complexes **1** and **2**

Cmpd	**1**					**2**			
				Q[a]					
EPR band	X	Q	X	(i)	(ii)	X	Q	X	Q
T [K]	300	180	90	10.5	10.5	300	300	91	11
g_1	2.029	2.048	2.035	1.950	2.000	2.059	2.053	2.060	2.012
g_2	2.071	2.040	2.063	2.029	2.032	2.059	2.053	2.062	2.067
g_3	2.259	2.258	2.258	2.289	2.267	2.32	2.307	2.185	2.349
$[g_3 - g_1]$	0.230	0.210	0.223	0.339	0.267	0.261	0.254	0.125	0.337
A_1	−4.79	2.739	−3.33	23.34	23.35	−1.756	−0.0002	−0.0002	36.69
A_2	−0.37	−25.47	3.2×10^{-5}	−0.116	0.0001	−0.232	0.0034	0.0002	−60.04
A_3	179.73	184.5	187.52	206.8	206.8	128.7	141.7	102.80	240.2
Lwpp [mT]	10.022	12.21	10.98	15.98	13.19	6.35	8.95	6.39	18
RMSD[b]	0.005	0.011	0.010	0.056	0.07	0.031	0.032	0.028	0.11

[a] The SH parameters fitted to Q-band spectra at 10.5 K for: (i) a bimodal signal without constraints yielding the g_1 value lower than 2.000 and (ii) for a monomodal signal with constraint of minimum g_1 value set at 2.000. For explanations, see text. [b] All fittings were performed several times for each case, starting from different input data, and as a result, similar final values were obtained with an accuracy of 3%. Hence, the final results were selected taking into account the best fits, i.e. those with the lowest RMSD value.

vs. broad signal, respectively) excludes the existence of unintentional impurities. Also, the reversibly of this signal can be observed only at very low temperatures (*ca.* below 25 K). In addition, values of the *g*-factors below 2.00 (from 1.86–1.99 from 4.5–12.5 K) might suggest formation of radical of different nature *i.e.*, not associated with the Cu(II) ion. Literature survey suggests that this signal may be due to the formation of Cu(I)-NO nitrosyl complexes, which were considered both theoretically and experimentally in zeolite matrices and small molecule complexes.[85–88] Formation of small fractions of Cu(I)NO species can be tentatively explained, when we assume that the isoxazole coordinating arms can participate in the Cu(II) > Cu(I) electron transfer. Graphical representation of the origin of the presumed Cu(I)NO nitrosyl-related radicals is depicted in Scheme S1.† Note that electronic structure calculations (Section 2.9.1) also suggest that existence of closely lying states of Cu(I) species may be feasible.

In the $S = \frac{1}{2}$ systems, where the ZFS parameters, *e.g.* the axial *D*, are not allowed, the magnetic anisotropy is due only to the anisotropy of the *g*-factors, *i.e.* the $[g_z - g_x]$ difference.[60] The values (Table 2) for **1** and **2** are three times higher than for the related system presented in the literature, which indicates that it can be exploited in quantifying the magnetic anisotropy. Nevertheless, since at liquid helium temperatures $[g_z - g_x]$ values are similar for **1** and **2**, it is not the only parameter that should be considered to explain the magnetic behavior (with magnetic relaxation being much longer for **1** than in **2**). One can also observe that temperature significantly affects the g_{eff} factor (Fig. S20†) and the EPR line width B_{pp} (Fig. S21†) for both compounds down to the liquid helium temperatures.

2.7 Theoretical calculations of spin Hamiltonian parameters

Using PHI program[79] we simulated EPR spectra and variation of electronic levels with external magnetic field for complex **1**. To simulate Cu(II) ion we set spin *S* as $\frac{1}{2}$ and orbital quantum number *L* as 2. Spin Hamiltonians (SH) parameters (Section 2.9) were calculated using MOLCAS[89] and we take g_x = 2.0660, g_y = 2.0920, g_z = 2.3810 from NEVPT2 calculations (Section 2.9). Temperature was set at 300 K, field frequency at 10 GHz (X-band), field was swept from 0.25 to 0.4 Tesla and was directed along the *x*-, *y*-, and *z*-axis of ***g***-tensor as well as powder integration was used. We used anisotropic spectra line widths to get better resemblance to experimental fits. Observed anisotropic broadening (Fig. S23 and S24†) might correspond to unresolved spectral features such as hyperfine coupling[90,91] and correlates with the experimentally observed structures.

2.8 Optical spectroscopy

To gain more insight into the electronic levels of **1** and therefore the nature of observed slow magnetic relaxation, optical spectroscopy and superposition model (SPM) calculations (Section 2.10) were performed. Fig. S25† shows the absorption spectrum measured at RT for complex **1**. The intense bands observed in the range of 22 000–50 000 cm^{-1} are associated with ligand-centered transitions. Electronic transitions of Cu(II) ions are much less intense than those associated with ligand absorption. They appear clearly for a more concentrated sample (blue line) and are observed in the range of 12 000–21 000 cm^{-1}. Fig. 6 (top) shows the absorption spectrum recorded in the range of Cu(II) electronic transitions at 4.2 K. Two bands at approximately 14 600 cm^{-1} and 17 300 cm^{-1} and a shoulder at approximately 12 600 cm^{-1} are clearly visible. Based on the above reasoning (details are in Section IV in ESI†) and the results of *ab initio* calculations (Section 2.9) the following energy level sequence can be proposed for Cu(II) in **1** assuming approximate C_2 symmetry: $^2A_2(d_{x^2-y2} + d_{z^2}) < {}^2A(d_{z^2} + d_{x^2-y^2}) < {}^2A(d_{xy}) < {}^2B(d_{xz} + d_{y,z}) < {}^2B(d_{xz} + d_{y,z})$ (Fig. 6 (bottom)). Accordingly, to the proposed energy levels structure four bands are expected in absorption spectrum of **1**. Deconvolution of the experimental spectrum using four Gaussian functions is presented in the inset in Fig. 6 (top). The obtained bands with maxima at 12 743, 14 441, 17 073 and 18 056 cm^{-1} correspond to transitions from the ground $^2A_2(d_{x^2-y^2} + d_{z^2})$ level to the $^2A(d_{z^2} + d_{x^2-y^2})$, $^2B(d_{xz} + d_{y,z})$, $^2B(d_{xz} + d_{y,z})$ and $^2A(d_{xy})$ excited levels. The value of *Dq* in the O_h approximation can be estimated as the difference between the average energy of levels arising from $T_{2g}(O_h)$ and $E_g(O_h)$ states. This yields a value of $Dq \sim 1015$ cm^{-1}, which seems to be reasonably acceptable. For complex **2** the RT absorption spectrum is practically the same as for complex **1** (Fig. S28†). Therefore, for the purpose of present analysis we

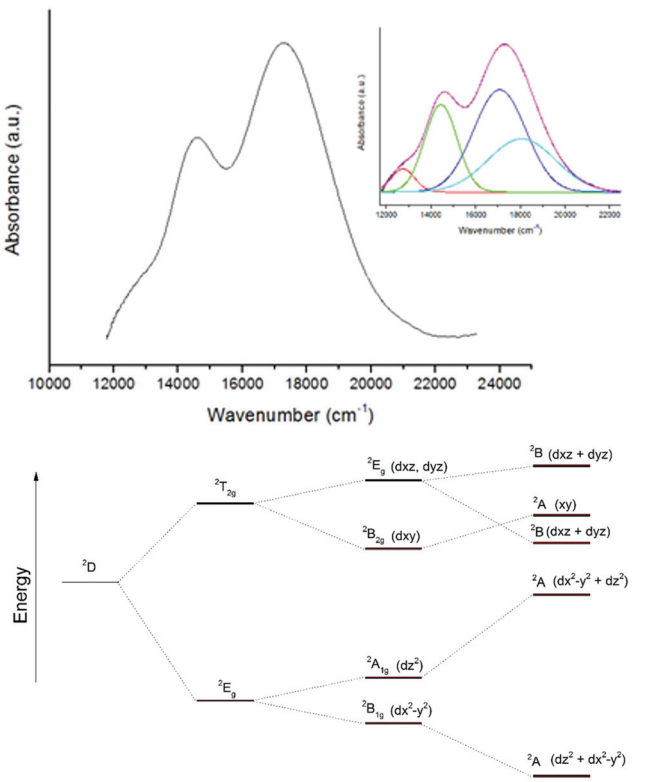

Fig. 6 (top) Absorption spectrum of **1** in the range of Cu(II) electronic transitions at 4.2 K; (bottom) energy level diagrams for Cu(II) ion as a function of symmetry changes.

accepted the same energy level structure for complexes **1** and **2**. The determined limiting values of *Dq*, *i.e.* 1015 and 1285 cm^{-1} were used in SPM analysis (Section 2.10).

2.9 Computations using *ab initio* methods

The *ab initio* methods cannot explain or provide direct information on magnetic relaxation processes or specific chemical aspects. However, there is a rationale for carrying out the *ab initio* computations due to three advantages. (1) They may assure that the predicted electronic structure of complexes **1** and **2** as well as so-computed spin Hamiltonian and/or ligand (crystal) field Hamiltonian parameters are compatible with those obtained by other methods. (2) The *ab initio* computed spin Hamiltonian (SH) parameters (*e.g.* the ***g***-tensor components) and the crystal/ligand field (CF/LF) ones may be used as starting parameters for fitting of various experimental data. (3) The *ab initio* computed CF/LF parameters may serve as input for independent modelling of the energy levels and thus SH parameters. Below we present only key results, whereas details of *ab initio* computations carried out using several methods are provided in Section VI in ESI.†

2.9.1 Electronic structure calculations. B3LYP solutions of total spin $S = \frac{1}{2}$ of Cu(II) ions of relevance to the magnetic properties are presented in Section VI in ESI.† This includes Mulliken populations (Table S10†) and Loewdin and Mayer analysis[92] (Table S11†). Analysis of the B3LYP results indicates what follows. Charges on the chemically equivalent N atoms are essentially the same for **1** and **2**, whereas main differences arise from the O atoms. O7 and O14 atoms are responsible for the axial structural distortions (Sections 2.3 and 2.10) and slightly lower charges in **1** than in **2**. The biggest difference in charge comes from the coordinated solvent molecules, with MeOH (**1**) translating to lower charge than H_2O (**2**). This comes from the inherent basicity of the molecule *per se*, but also from the H-bonding pattern that differs within the synthesized systems (Section 2.2). For experimental structure of complex **2** it was not possible to get the magnetic solution with spin localized at the Cu center. Cu atom is nonmagnetized with small leakage of charge (+0.3863|*e*|). This corresponds more closely to $S = 0$ and Cu(I) oxidation state than to Cu(II; $S = \frac{1}{2}$), nonetheless Cu(II) are known to be inherently more stable than Cu(I) complexes, the latter being prone to oxidation. We did however observe low-temperature helium EPR signals (Section 2.6) that could speculatively suggest formation of small amounts of Cu(I)NO moieties, thus explaining the observed magnetic solution. Only after optimization of geometric structure we obtained magnetic state with localized magnetic moment but during the process of geometry optimization the bond between Cu and H_2O is broken and coordination number changes from 6 to 5. This suggest that there might be close-lying states with different valence properties and geometrical structures.

Excited states were computed for complex **1** using TDDFT with long-range corrected exchange–correlation functional CAM-B3LYP. Results of representative multiconfigurational-SCF calculations are provided below, whereas computational details and detailed results are provided in Section VI in ESI.† Calculations were performed using CASSCF method with additional perturbations NEVPT2 to account for dynamic correlations. For Cu(II) ion we choose the active space consisting of five orbitals with major contribution of 3d atomic states with 9 electrons that could occupy them. The self-consistent procedure yields five states well separated from each other in energy scale, *i.e.* orbital singlets (Table 3).

Calculations for complex **1** show that the ground state consists of total 9 3d electrons in two major configurations: (i) with unpaired $3d_{z^2}$ electron (~70%) and (ii) with unpaired $3d_{x^2-y^2}$ electron (~29%). The 1st excited state is similar to the ground state but proportions are nearly inverted for (ii) with unpaired $3d_{x^2-y^2}$ electron (~68%) and (i) with unpaired $3d_{z^2}$ electron (~29%). Other excited states correspond to the following configurations: 2nd – with unpaired $3d_{xz}$ electron, 3rd – with unpaired $3d_{xy}$ electron, and 4th – with unpaired $3d_{yz}$ electron. Calculations for complex **2** show that the ground state consists of total 9 3d electrons in two major configurations: (i) with unpaired $3d_{z^2}$ electron (~77%) and (ii) with unpaired $3d_{x^2-y^2}$ electron (~22%). The 1st excited state consists of two configurations: (i) with unpaired $3d_{xz}$ electron (~51%) and (ii) with unpaired electron $3d_{x^2-y^2}$ (~39%). The 2nd excited state is similar to the 1st excited state but proportions are different for (ii) with unpaired $3d_{x^2-y^2}$ electron (~37%) and (i) with unpaired $3d_{xz}$ electron (~42%). Other excited states correspond to the following configurations: 3rd – with unpaired $3d_{yz}$ electron and 4th – with unpaired $3d_{xy}$ electron. The 3rd and 4th excited state are well separated, suggesting that structure **2** is geometrically more distorted than structure **1**.

The effects of the inclusion of NEVPT2 dynamic corrections for the energy levels and the excited states for complex **1** are discussed Section VI in ESI.† Comparative analysis of these effects and the DFT results indicates what follows. The MC-SCF Mulliken occupations of the selected atoms show some differences with respect to DFT results. Most important is the fact that the spin is more strongly localized at the Cu site and electronic charge is closer to nominal charge 2+ (Table S10†). Charges on atoms neighboring with Cu are larger

Table 3 Energies of the excited states w.r.t. the ground state (in cm^{-1}) calculated using CASSCF and NEVPT2 for complex **1** and **2**

Excited state	CASSCF **1**	NEVPT2 **1**	CAM-B3LYP TDA **1**	CASSCF **2**	NEVPT2 **2**
1st	9699	12 680	12 574	9972	12 282
2nd	10 420	14 255	17 761	10 547	14 048
3rd	12 212	16 186	17 907	12 134	16 421
4th	12 262	16 215	18 578	13 228	18 030

than those obtained from DFT. Spins on these neighboring atoms are very small. This finding is also supported by Loewdin analysis (Table S14†). Nonrelativistic CASSCF excited states are well separated from the ground state and this separation is significantly enlarged with inclusion of dynamic correlations at NEVPT2 level. Consequences of the enlarged separations of states are discussed in Section VI in ESI.†

2.9.2 Calculations of the spectroscopic splitting factors *g*. The ***g***-tensor components (g_x, g_y, g_z) were calculated in the principal axis system (PAS) using ZORA approach (Table 4 and Table S17†).

Results indicate large difference between g_z and (g_x, g_y), whereas g_x and g_y differ slightly since our system has C_1 symmetry. The main magnetic axes, which correspond to the PAS of Zeeman Hamiltonian,[93] do not exactly correspond to the molecular bonds of Cu and neighboring atoms but are lying closely. CASSCF method overestimate the *g*-factors with respect to NEVPT2 method, so (g_i) components derived from the latter one conform well to experimental data for axial symmetry Cu (II) systems.[94–97] We have also listed B3LYP results with the basis aug-cc-pVTZ-J and CP(PPP) for Cu atom with extra fineness of the grid to get more accurate values of the *g* tensor. Products of magnetic susceptibilities and temperature $\chi T = \partial^2 E/\partial B^2$ for complexes **1** and **2** obtained using NEVPT2 are plotted in Fig. S29.† Plots of EPR spectra (Fig. S23, S24† and Section 2.7) obtained using MOLCAS[89] and PHI[79] support the conclusion that hyperfine structure might be important in such simulations.

2.10 SPM and MSH analysis

The rationale for employing the two semiempirical modelling approaches, *i.e.* SPM and MSH, are two-fold. (1) To complement and corroborate (a) the spin Hamiltonian parameters obtained experimentally by EPR (Section 2.6) and computationally by DFT/*ab initio* approaches (Section 2.9) as well as (b) CF parameters (CFPs) estimated experimentally by optical spectroscopy (Section 2.8). This would enhance reliability of the overall results. (2) To gain more insight into magneto-structural correlations and thus explain differences in magnetic character of compounds **1** and **2**. The results of calculations carried out to fulfil rationale (1) are presented below, whereas those concerning rationale (2) are discussed in Section 3.

For initial estimation of the g_i factors, simplified MSH formulas listed in Section VII† were employed.[98,99] The results have indicated general suitability of the MSH approach. For more accurate calculations of SHPs, the MSH formulas for tetragonal (TE)[100–106] and orthorhombic[107–109] symmetry is applied. To obtain input data for MSH formulas, the CFPs B_{kq}[110–112] are calculated using SPM for Cu(II) centers in **1** and **2** using the structural data for set C_{2v} (Section V in ESI†). The two plausible *Dq* values ~1015 cm^{-1} and ~1285 cm^{-1} estimated by us experimentally from optical spectra (Section 2.8) are adopted. Pertinent comments on reliability of usage of SPM/CFP predictions as input data for MSH formulas are provided in Section VII in ESI.† The results listed in Table 5 indicate that after standardization (see Section VII in ESI†) the axial CFP B_{20} of the highest magnitude and minimal values of B_{22} and B_{42} are obtained, while B_{20} and B_{22} also change signs along the choice of positive rhombicity ratio built into CST package.[113,114]

The relations between the CF energy levels in eqn (S6) and (S7) and those E_1 and E_2 employed in MSH formulas for tetragonal symmetry in ref. 101 and 104 are as follows:

$$E_1 = 10Dq = \Delta E = (|d_{x^2-y^2}\rangle - |d_{xy}\rangle)$$

$$E_2 = 10Dq - 3Ds + 5Dt = \Delta E = (|d_{x^2-y^2}\rangle - |d_{yz}\rangle) = \Delta E = (|d_{x^2-y^2}\rangle - |d_{xz}\rangle) \quad (6)$$

In eqn (6) *Dq* denotes the cubic CFP, whereas *Ds* and *Dt* denote the second- and fourth-rank tetragonal CFPs in the conventional notation,[117,118] respectively. Depending on the shape of the distorted octahedron (Section 2.3) and thus the strength of tetragonal CFPs, the ground state may be either $|d_{x^2-y^2}\rangle$ or $|d_{z^2}\rangle$.[98,99] This is also evident in our *ab initio* calculations (Section 2.9). Next, using the CFPs in Table 5 and the

Table 4 The ***g***-tensor components for complexes **1** and **2** in the principal axis system (PAS) using ZORA approach

g-Tensor	CASSCF **1**	NEVPT2 **1**	CASSCF **2**	NEVPT2 **2**	B3LYP DFT **1**
g_x	2.081	2.067	2.074	2.058	2.048
g_y	2.115	2.093	2.113	2.087	2.054
g_z	2.517	2.386	2.511	2.409	2.177

Table 5 The CFPs in Wybourne notation B_{kq} (in cm^{-1}) calculated using SPM with $Dq \sim 1285$ cm^{-1} and $Dq \sim 1015$ cm^{-1} for set C_{2v}

	Complex **1**				Complex **2**			
CFPs	C_{2v}		C_{2v} after OR/ST[a]		C_{2v}		C_{2v} after OR/ST[a]	
Dq	1285	1015	1285	1015	1285	1015	1285	1015
B_{20}	15 931	12 584	−28 719	−22 685	16 017	12 651	−26 735	−21 118
B_{22}	16 945	13 385	−1283	−1014	15 290	12 078	−2163	−1708
B_{40}	31 528	24 889	21 424	16 913	30 963	24 443	21 239	16 767
B_{42}	−8102	−6396	−1712	−1351	−7429	−5864	−1279	−1010
B_{44}	15 305	12 082	23 758	18 756	14 822	11 701	22 958	18 123

[a] The orthorhombic transformation (OR/ST) defined as S2:[109,113,115,116] $(X, Y, Z) \rightarrow (X, -Z, Y)$ was applied.

conversion relations between the CFPs B_{kq} and (Ds, Dt) given in ref. 118, the latter CFPs are calculated, and subsequently, the energies E_1 and E_2 in eqn (6). Finally, the tetragonal SHPs: g_i and A_i are calculated by applying the respective MSH formulas.[101,104] To calculate the hyperfine structure parameters A_i we employ analogous MSH formulas derived as functions of the g_i values and respective CF energies.[100–106]

For orthorhombic symmetry,[107–109] four CF energies E_i (i = 1–4) apply. The corresponding relations are:

$$E_1 = 10Dq$$

$$E_2 = 10Dq + 3Ds - 5Dt - 3D_\xi + 4D\eta^2$$

$$E_3 = 10Dq + 3Ds - 5Dt + 3D_\xi - 4D\eta^2$$

$$E_4 = -4Ds - 5Dt \quad (7)$$

in eqn (7) Dq, Ds and Dt have the same meaning as in eqn (6), whereas D_ξ and D_η are the conventional orthorhombic CFPs, which are related to the CFPs B_{kq}. The orthorhombic (OR) SHPs g_i and A_i calculated applying the respective MSH formulas[107–109] are listed in Table S19.† To facilitate comparison of the orthorhombic g_i and A_i components and the perpendicular tetragonal ones, the averaged values: $(g_x + g_y)/2 \sim g_\perp$ and $(A_x + A_y)/2 \sim A_\perp$ are also calculated, while the axial components are directly comparable: $g_z \sim g_\parallel$ and $A_z \sim A_\parallel$.

Three important points bearing on interpretation of results in Table S19† must be kept in mind as discussed in Section VII in ESI.† In view of these points, analysis of the results in Table S19† leads to the following conclusions. The SHPs g_i and A_i calculated using MSH formulas for the TE case may be directly compared with experimental results in Section 2.3, whereas those for the orthorhombic (OR) case – with the *ab initio* results in Section 2.9. Results for both cases indicate good mutual consistency, which shows the usefulness of the ascent/descent in symmetry.[119–121] Employing the standardized CFP sets in MSH calculations is even more crucial in the TE case than in the OR case, in view of additional approximations involved in the TE case, *i.e.* omitting the orthorhombic CFPs: B_{22} and B_{42}.

The values of g_i calculated in Table S19† by adopting TE and OR formulas agree well with our experimental ones: $g_\parallel$ = 2.26 and $g_\perp$ = 2.05 for complex **1** and also with literature data obtained for compounds with axial symmetry Cu-sites, see Table S20.† Since EPR spectra were done on powdered samples, the axes (x, y, z) indicated for the fitted values, *i.e.* $g_\parallel$ (z), $g_\perp$ (x, y), may be considered only as the nominal principal axes. Hence, they cannot be related the orientations of any specific axes within the coordination octahedron (Fig. 1c and d). Comparison of the theoretical A_i values in Table S19† with our experimental value $A_\parallel$ = 175 (G) = 165.8 (10^{-4} cm^{-1}) for complex **1** and the respective values in Table S20† reveals that all experimental $A_\parallel$ are positive, whereas theoretical ones are negative. This is due to the limited capabilities of the computer program used, have allowed fitting EPR spectra only with the absolute values of the hyperfine interaction parameters $|A|$. Since no perpendicular splitting has been observed in EPR spectrum, no accurate value of $A_\perp$ could be determined. Attempts to simulate spectra using $A_\perp$ indicate that this is not a sensitive parameter because any splitting is hidden in the main EPR line. A good match has been obtained with $A_\perp$ equal 1 as well as 20 cm^{-1}. Both formulas: TE and OR ones, yield comparable sets of results and indicate that good agreement may be obtained by appropriate matching of the adjustable parameters. However, overall the Dq value (in cm^{-1}) 1015 seems better than 1285, which yields larger CF energies (E_i). This finding conforms to that obtained in Section 2.8. Comparison of the TE and OR results for sets C_{2v} or both complexes **1** and **2** in Table S19† indicates smaller differences between the respective results than those for sets C_{2v} after OR/ST. This may be due to the approximations involved in the TE case. Since no such approximations are involved in the OR case, the results for sets C_{2v} after OR/ST may be considered as more accurate. Comparison of the results in Table S19† and the respective results obtained by *ab initio* methods (Section 2.9) also favor the MSH results obtained with lower Dq value for sets C_{2v} after OR/ST. Importantly, the CF energies obtained for sets C_{2v} do not agree as well those for sets C_{2v} after OR/ST. This reinforces the importance of employing orthorhombic standardization.

3. Magneto-structural correlations and outcome

Results provided in Section 2 and in ESI† enable us to extract some information on correlation between the chemical composition of **1** and **2** and their magnetic relaxation properties. The following dependencies were observed in this study. Slow relaxation of magnetization is observed only in the presence of the external magnetic field and it mostly concerns compound **1** [Cu(**Lred^1**)(MeOH)](ClO$_4$)$_2$, while it is much less pronounced in compound **2** [Cu(**Lred^2**)(H$_2$O)](OTf)$_2$. Each metal ion is isolated in its crystal lattice without any exchange interactions, as confirmed by X-ray structures (Cu⋯Cu distances over 8 Å), DC magnetic and EPR studies. This means that observed differences can be related to variations in symmetry of Cu(II) ion in CuL$_n$ complex, secondary coordination sphere, and/or additional crystal packing effects.

Structural similarity of the [CuN$_3$O$_3$] coordination octahedron (N$_3$O square planar plane and O$_2$ axial elongation – see, Scheme 1) is retained in both complexes, despite differences in the composition of ligands **Lred^1** and **Lred^2** and coordinated solvent molecule. Axial octahedral elongation is stronger in **1** than in **2** as determined by SHAPE studies (Section 2.3) and the differences are also observed in temperature-dependent cw-EPR studies (Section 2.6). This phenomenon can be attributed to the Jahn–Teller distortions, which were extensively studied to show structural and electronic consequences of the Jahn–Teller effect.[122] Present axial elongation leads to an anisotropic distribution of d-electron spins, which has huge impact on magnetic properties. The N$_3$O plane is

more distorted from the pure square planar one in **2** than in **1** (Section 2.3), whereas the excited state calculations also point to this symmetry deviation (Section 2.9.1). Overall, symmetry of compound **1** is akin those of porphyrins/phthalocyanines, which facilitate SIM/qubit behavior for symmetry reasons.[50–55] The charge analysis of the ground state of Cu^{2+} ions in complex **1** and **2**, indicates that the CASSCF/NEVPT2 state energies and g_i factors are typical for an octahedrally distorted copper(II) complexes. The conclusions drawn from CASSCF calculations are corroborated by TD-DFT and semiempirical results as well as are consistent with level schemes for low symmetries reported in literature.[98]

To fulfil the rationale (2) of semiempirical calculations (Section 2.10), we examine the dependence of the SPM calculated CFPs on the structural parameters of the complexes, *e.g.* bond lengths, R_i. This enables to gain insight on how the changes in CFPs affect the MSH calculated SHPs: g_i and A_i. An increase in R_i values results in a decrease in E_i values in both TE and OR symmetry cases. This in turn induces a decrease in $g_\perp$ but an increase in $g_\parallel$ values. Similar trend is also observed for $A_\perp$ and $A_\parallel$, respectively. Computations also reveal that the reason for the differences in the properties of both complexes **1** and **2** may not be solely related to the immediate surroundings of the Cu(II) ions and other factors, *e.g.* solid state packing may play a role as discussed below.

In the solid state, both complexes show two molecules of crystallographically equivalent but magnetically inequivalent compounds (C_2 inversion axis) in the unit cell. Interestingly, only in **1** they symmetrically interact with each other in antiparallel manner through the pyridine–pyridine π–π stacking interactions (Fig. S22†), similarly as reported.[59,123] This ensures the rigid crystal packing, which is otherwise more loose in compound **2**, which is related to the effect of the counterion involved in the H-bonded packing (ClO_4^- in **1**, $CF_3SO_3^-$ in **2**). The molecular structure of both compounds is not devoid of high-energetic vibrations (C–H, NH) that may also contribute to relaxation mechanisms considered here, *i.e.* of Raman, direct and QTM origin (Section 2.5). Boča *et al.*[60] showed that octahedral [Cu(pydca)(dmpy)]·0.5H_2O (where pydca – pyridine-2,6-dicarboxylate, dmpy – 2,6-dimethanolpyridine) exhibits two relaxation processes with energy barriers estimated as U/k_B = 58.6 and 62.7 K. This may be due to existence of two distinct Cu(II) centers in the crystal lattice, each with different local site symmetry Cu(II). Boča's group[59] also showed that monometallic octahedral [CuLL′$_2$(H_2O)] complex (where L = 2,6-dimethanolpyridine and L′ = 3,5-dinitrocarboxylate) forms dimers that are arranged in the π–π stacking. This leads to 1D-chain and/or ladder structure that also exhibits two relaxation processes through the direct and Raman-like contributions. Cui *et al.*[61] showed that five-coordinate [Cu(12-TMC)Cl][B(C_6H_5)$_4$] (12-TMC = 1,4,7,10-tetramethyl-1,4,7,10-tetraaza cyclododecane) exhibits only one relaxation process in a distorted square pyramidal geometry of copper(II) ion. Korchagin *et al.*[62] demonstrated that the quasi-one-dimensional Cu(II) complex [Cu(hfac)$_2$(ClTDPO)]$_n$ (where hfac – hexafluoroacetylacetonate, ClTDPO – 2,4-di-(*tert*-butyl)-9-chlorobenzo[5,6][1,4]oxazine[2,3-*b*]phenoxazine) relaxes through the combination of two-phonon Raman and one-phonon direct processes. Since these examples represent mutually unrelated compounds, more studies of structurally similar monometallic Cu(II) systems are needed to better understand the observed phenomena.

4. Conclusions

Our study provides solid grounds for development of a modular organic platform for controlled formation of magnetically isolated, monometallic Cu(II) systems. This approach would enable better understanding of magnetic relaxation behaviour in $S = \frac{1}{2}$ systems. Herein, the tunable capability of the synthesized complexes comes from: (i) the unique pentadentate **Lred^{1}R** *N*,*O*-aminal ligand family formed by unexpected *in situ* reduction of the parent Schiff base ligand **L**; (ii) the chosen solvent/reagent alcohol; (iii) the coordination preferences of the metal salt and its counterion. Since the field-induced SIM coordination compounds with d^9 ions are rarely encountered, two structurally similar octahedral Cu(II) compounds were prepared as the case study. The above aspects (i) and (ii) affect modularity most significantly. Both analogues are rare examples of magnetically isolated copper systems that display slow relaxation of magnetisation, with phenomenon being more pronounced for the perchlorate analogue **1** than the triflate **2**.[48]

Experimental findings indicate that this behaviour is predominantly the result of: (i) the octahedral structural distortions exerted by the alkoxy groups appended on the $\mathbf{L}^{\mathbf{red\text{-}1/2}}$ scaffold; (ii) spatial arrangements of the Cu(II)···Cu(II) pairs in the unit cell due to the crystal packing contacts, with anion and π–π interactions being the most important. This translates to the character of the hyperfine structure observed in the EPR spectra as a function of temperature and applied frequencies, related to the interactions of $S = \frac{1}{2}$ electron spin of Cu(II) ion with the nuclear spin I = 3/2. The relaxation of magnetization proceeds through the combination of Raman, direct and QTM processes.

The extensive *ab initio* ((TD-)DFT, CASSCF, NEVPT2) computations and semiempirical (SPM, MSH) calculations have included the following aspects. Cu(II) electronic states, ***g***-tensor and ***A***-tensor components as well as ligand field parameters were calculated and compared with the experimentally determined values. This enables to gain insight on how the changes in CFPs affect the MSH calculated SHPs: g_i and A_i. Such thorough and combined strategy allowed us to probe the effect of geometrical and structural changes on copper(II) electronic states. Consequently, our investigations provided better understanding of the observed magnetic behaviour. The theoretical results corroborate experimental findings and are consistent with level schemes for low symmetries reported in literature.

The thorough and combined strategy, utilized for two Cu(II) ion complexes for the first time, has also helped to delineate

advantages and limitations of each of the several experimental techniques and theoretical approaches employed. Hence, this combined strategy may guide development of the design of other potential Cu(II)-based nanomagnets as well. Additional aspects concerning modularity in our study may be invoked, *e.g.* strongly coordinating counterions. Interestingly, demonstrated modular character of alkoxy groups would allow one to attach perfluorinated arms to evaluate the role of aliphatic CH_2 and CH_3 vibrations on the relaxation behaviour in the future. These aspects, together with the role of secondary coordination sphere on magnetic relaxation mechanisms are currently of particular interest.[124]

Author contributions

Dawid Marcinkowski: synthesis of chemical compounds, magneto-structural correlations: conceptualization, methodology, formal analysis, investigation, resources, data curation, writing – original draft, writing – review & editing, visualization. Ariel Adamski: synthesis of chemical compounds: conceptualization, methodology, formal analysis, investigation, resources, data curation, writing – review & editing, visualization. Maciej Kubicki: crystallographic studies: formal analysis, investigation, data curation, writing – review & editing, visualization. Giuseppe Consiglio: synthesis of chemical compounds: formal analysis, investigation, data curation, writing – review & editing. Violetta Patroniak: methodology, formal analysis, investigation, writing – review & editing, supervision. Tomasz Ślusarski: theoretical studies: DFT/*ab initio* calculations, formal analysis, investigation, data curation, writing – review & editing, visualization. Muhammed Açıkgöz: theoretical studies: SPM and MSH calculations, formal analysis, investigation, data curation, writing – review & editing, visualization. Daria Szeliga: DC/AC magnetism studies: formal analysis, investigation, data curation, writing – review & editing, visualization. Nahir Vadra: magneto-structural correlations: data curation, writing – review & editing, visualization. Mirosław Karbowiak: spectroscopic and theoretical studies: conceptualization, methodology, formal analysis, investigation, resources, data curation, writing – review & editing, visualization. Ireneusz Stefaniuk: EPR studies: conceptualization, methodology, formal analysis, investigation, resources, data curation, writing – review & editing, visualization. Czesław Rudowicz: magneto-structural correlations, analysis of SPM, MSH and DFT/*ab initio* results, conceptualization, methodology, formal analysis, investigation, resources, data curation, writing – review & editing, visualization, supervision, funding acquisition. Adam Gorczyński: SHAPE symmetry studies, magneto-structural analysis and correlations: conceptualization, methodology, formal analysis, investigation, resources, data curation, writing – original draft, writing – review & editing, visualization, supervision. Maria Korabik: DC/AC magnetism studies: conceptualization, methodology, formal analysis, investigation, resources, data curation, writing – review & editing, visualization, supervision.

Conflicts of interest

There are no conflicts to declare.

Acknowledgements

Dedicated to Professor Stefan Lis on the occasion of his 70th birthday. Technical assistance with EPR measurements from MSc B. Cieniek is much appreciated. This work was mainly supported by: (PI: CZR): UMO-2016/21/B/ST4/02064 from the Polish National Science Center and partially from the budget for science in 2018–2020, as a part of the Polish Ministry of Science and Higher Education project; (PI: DM): Grant No. 0088/DIA/2018/47 in the frame of the "Diamond Grant" programme; (PI: AG): SONATA grant UMO-2020/39/D/ST4/01182 from National Science Centre, Poland. A. G. is a scholarship holder of the Polish Ministry of Education and Science for outstanding young scientists. D. M. is a scholarship holder of the Adam Mickiewicz University Foundation for the academic year 2021/2022. The calculations were made at the Poznań Supercomputing and Networking Center.

References

1 E. Coronado, *Nat. Rev. Mater.*, 2020, **5**, 87–104.
2 C. A. P. Goodwin, *Dalton Trans.*, 2020, **49**, 14320–14337.
3 A. Zabala-Lekuona, J. M. Seco and E. Colacio, *Coord. Chem. Rev.*, 2021, **441**, 213984.
4 C. E. Jackson, I. P. Moseley, R. Martinez, S. Sung and J. M. Zadrozny, *Chem. Soc. Rev.*, 2021, **50**, 6684–6699.
5 R. Mirzoyan, N. P. Kazmierczak and R. G. Hadt, *Chem. – Eur. J.*, 2021, **27**, 9482–9494.
6 M. S. Fataftah and D. E. Freedman, *Chem. Commun.*, 2018, **54**, 13773–13781.
7 M. Affronte, *J. Mater. Chem.*, 2009, **19**, 1731–1737.
8 E. Moreno-Pineda and W. Wernsdorfer, *Nat. Rev. Phys.*, 2021, **3**, 645–659.
9 K. Head-Marsden, J. Flick, C. J. Ciccarino and P. Narang, *Chem. Rev.*, 2021, **121**, 3061–3120.
10 K. S. Pedersen, A.-M. Ariciu, S. McAdams, H. Weihe, J. Bendix, F. Tuna and S. Piligkos, *J. Am. Chem. Soc.*, 2016, **138**, 5801–5804.
11 A. Gaita-Ariño, H. Prima-García, S. Cardona-Serra, L. Escalera-Moreno, L. E. Rosaleny and J. J. Baldoví, *Inorg. Chem. Front.*, 2016, **3**, 568–577.
12 M. Atzori and R. Sessoli, *J. Am. Chem. Soc.*, 2019, **141**, 11339–11352.
13 A. Gaita-Ariño, F. Luis, S. Hill and E. Coronado, *Nat. Chem.*, 2019, **11**, 301–309.
14 C.-J. Yu, S. von Kugelgen, D. W. Laorenza and D. E. Freedman, *ACS Cent. Sci.*, 2021, **7**, 712–723.
15 S. E. Crawford, R. A. Shugayev, H. P. Paudel, P. Lu, M. Syamlal, P. R. Ohodnicki, B. Chorpening, R. Gentry

and Y. Duan, *Adv. Quantum Technol.*, 2021, **4**, 2100049–2100082.
16 S. Krastanov, M. Heuck, J. H. Shapiro, P. Narang, D. R. Englund and K. Jacobs, *Nat. Commun.*, 2021, **12**, 191.
17 R. S. D. Gatteschi and J. Villain, *Molecular Nanomagnets*, Oxford University Press, Oxford, 2006.
18 F. L. J. Bartolomé and J. F. Fernández, *Molecular Nanomagnets: Physics and Applications*, Springer-Verlag Berlin, Heidelberg, 2014.
19 D. G. C. Benelli, *Introduction to Molecular Magnetism: From Transition Metals to Lanthanides*, Wiley-VCH, Weinheim, 2015.
20 R. A. Layfield, M. Murugesu, *Lanthanides and Actinides in Molecular Magnetism*, Wiley-VCH, Weinheim, 2015.
21 P. Z. J. Tang, *Lanthanide Single Molecule Magnets*, Springer-Verlag Berlin Heidelberg, 2015.
22 E. S. Gao, *Molecular Nanomagnets and Related Phenomena, Structure and Bonding*, Springer-Verlag Berlin, Heidelberg, 2015.
23 F.-S. Guo, B. M. Day, Y.-C. Chen, M.-L. Tong, A. Mansikkamäki and R. A. Layfield, *Science*, 2018, **362**, 1400.
24 C. A. P. Goodwin, F. Ortu, D. Reta, N. F. Chilton and D. P. Mills, *Nature*, 2017, **548**, 439–442.
25 F.-S. Guo, B. M. Day, Y.-C. Chen, M.-L. Tong, A. Mansikkamäki and R. A. Layfield, *Angew. Chem., Int. Ed.*, 2017, **56**, 11445–11449.
26 K. Randall McClain, C. A. Gould, K. Chakarawet, S. J. Teat, T. J. Groshens, J. R. Long and B. G. Harvey, *Chem. Sci.*, 2018, **9**, 8492–8503.
27 M. J. Giansiracusa, A. K. Kostopoulos, D. Collison, R. E. P. Winpenny and N. F. Chilton, *Chem. Commun.*, 2019, **55**, 7025–7028.
28 S. E. Stavretis, D. H. Moseley, F. Fei, H.-H. Cui, Y. Cheng, A. A. Podlesnyak, X. Wang, L. L. Daemen, C. M. Hoffmann, M. Ozerov, Z. Lu, K. Thirunavukkuarasu, D. Smirnov, T. Chang, Y.-S. Chen, A. J. Ramirez-Cuesta, X.-T. Chen and Z.-L. Xue, *Chem. – Eur. J.*, 2019, **25**, 15846–15857.
29 B. Yin and C.-C. Li, *Phys. Chem. Chem. Phys.*, 2020, **22**, 9923–9933.
30 A. Castro-Alvarez, Y. Gil, L. Llanos and D. Aravena, *Inorg. Chem. Front.*, 2020, **7**, 2478–2486.
31 Y.-Q. Zhai and Y.-Z. Zheng, *J. Mater. Chem. C*, 2021, **9**, 8096–8098.
32 L. Escalera-Moreno, J. J. Baldoví, A. Gaita-Ariño and E. Coronado, *Chem. Sci.*, 2018, **9**, 3265–3275.
33 E. Bartolomé, A. Arauzo, J. Luzón, J. Bartolomé and F. Bartolomé, in *Handbook of Magnetic Materials*, ed. E. Brück, Elsevier, 2017, vol. 26, pp. 1–289.
34 K. S. Pedersen, J. Bendix and R. Clérac, *Chem. Commun.*, 2014, **50**, 4396–4415.
35 M. Atzori, S. Benci, E. Morra, L. Tesi, M. Chiesa, R. Torre, L. Sorace and R. Sessoli, *Inorg. Chem.*, 2018, **57**, 731–740.
36 E. Coronado, *Nat. Rev. Mater.*, 2020, **5**, 87–104.
37 L. Tesi, E. Lucaccini, I. Cimatti, M. Perfetti, M. Mannini, M. Atzori, E. Morra, M. Chiesa, A. Caneschi, L. Sorace and R. Sessoli, *Chem. Sci.*, 2016, **7**, 2074–2083.
38 M. Atzori, E. Morra, L. Tesi, A. Albino, M. Chiesa, L. Sorace and R. Sessoli, *J. Am. Chem. Soc.*, 2016, **138**, 11234–11244.
39 M. Atzori, L. Tesi, S. Benci, A. Lunghi, R. Righini, A. Taschin, R. Torre, L. Sorace and R. Sessoli, *J. Am. Chem. Soc.*, 2017, **139**, 4338–4341.
40 A. Albino, S. Benci, L. Tesi, M. Atzori, R. Torre, S. Sanvito, R. Sessoli and A. Lunghi, *Inorg. Chem.*, 2019, **58**, 10260–10268.
41 M. Atzori, L. Tesi, E. Morra, M. Chiesa, L. Sorace and R. Sessoli, *J. Am. Chem. Soc.*, 2016, **138**, 2154–2157.
42 J. J. Scepaniak, C. S. Vogel, M. M. Khusniyarov, F. W. Heinemann, K. Meyer and J. M. Smith, *Science*, 2011, **331**, 1049.
43 G. E. Cutsail III, B. W. Stein, D. Subedi, J. M. Smith, M. L. Kirk and B. M. Hoffman, *J. Am. Chem. Soc.*, 2014, **136**, 12323–12336.
44 M. Ding, G. E. Cutsail III, D. Aravena, M. Amoza, M. Rouzières, P. Dechambenoit, Y. Losovyj, M. Pink, E. Ruiz, R. Clérac and J. M. Smith, *Chem. Sci.*, 2016, **7**, 6132–6140.
45 I. Bhowmick, A. J. Roehl, J. R. Neilson, A. K. Rappé and M. P. Shores, *Chem. Sci.*, 2018, **9**, 6564–6571.
46 R. C. Poulten, M. J. Page, A. G. Algarra, J. J. Le Roy, I. López, E. Carter, A. Llobet, S. A. Macgregor, M. F. Mahon, D. M. Murphy, M. Murugesu and M. K. Whittlesey, *J. Am. Chem. Soc.*, 2013, **135**, 13640–13643.
47 W. Lin, T. Bodenstein, V. Mereacre, K. Fink and A. Eichhöfer, *Inorg. Chem.*, 2016, **55**, 2091–2100.
48 R. Boča and C. Rajnák, *Coord. Chem. Rev.*, 2021, **430**, 213657.
49 C. Rajnák and R. Boča, *Coord. Chem. Rev.*, 2021, **436**, 213808.
50 M. Warner, S. Din, I. S. Tupitsyn, G. W. Morley, A. M. Stoneham, J. A. Gardener, Z. Wu, A. J. Fisher, S. Heutz, C. W. M. Kay and G. Aeppli, *Nature*, 2013, **503**, 504–508.
51 K. Bader, M. Winkler and J. van Slageren, *Chem. Commun.*, 2016, **52**, 3623–3626.
52 A. Urtizberea, E. Natividad, P. J. Alonso, M. A. Andrés, I. Gascón, M. Goldmann and O. Roubeau, *Adv. Funct. Mater.*, 2018, **28**, 1801695.
53 C.-J. Yu, M. D. Krzyaniak, M. S. Fataftah, M. R. Wasielewski and D. E. Freedman, *Chem. Sci.*, 2019, **10**, 1702–1708.
54 C.-J. Yu, S. von Kugelgen, M. D. Krzyaniak, W. Ji, W. R. Dichtel, M. R. Wasielewski and D. E. Freedman, *Chem. Mater.*, 2020, **32**, 10200–10206.
55 S. von Kugelgen, M. D. Krzyaniak, M. Gu, D. Puggioni, J. M. Rondinelli, M. R. Wasielewski and D. E. Freedman, *J. Am. Chem. Soc.*, 2021, **143**, 8069–8077.

56 Y. Dai, Y. Fu, Z. Shi, X. Qin, S. Mu, Y. Wu, J.-H. Su, Y.-F. Deng, L. Qin, Y.-Q. Zhai, Y.-Z. Zheng, X. Rong and J. Du, *Chin. Phys. Lett.*, 2021, **38**, 030303.
57 M. S. Fataftah, M. D. Krzyaniak, B. Vlaisavljevich, M. R. Wasielewski, J. M. Zadrozny and D. E. Freedman, *Chem. Sci.*, 2019, **10**, 6707–6714.
58 S. Lenz, K. Bader, H. Bamberger and J. van Slageren, *Chem. Commun.*, 2017, **53**, 4477–4480.
59 D. Valigura, C. Rajnák, J. Titiš, J. Moncoľ, A. Bieńko and R. Boča, *Dalton Trans.*, 2022, **51**, 5612–5616.
60 R. Boča, C. Rajnák, J. Titiš and D. Valigura, *Inorg. Chem.*, 2017, **56**, 1478–1482.
61 H.-H. Cui, W. Lv, W. Tong, X.-T. Chen and Z.-L. Xue, *Eur. J. Inorg. Chem.*, 2019, 4653–4659.
62 D. V. Korchagin, E. P. Ivakhnenko, O. P. Demidov, A. V. Akimov, R. B. Morgunov, A. G. Starikov, A. V. Palii, V. I. Minkin and S. M. Aldoshin, *New J. Chem.*, 2021, **45**, 21912–21918.
63 A. Mielcarek, A. Bieńko, P. Saramak, J. Jezierska and A. Dołęga, *Dalton Trans.*, 2019, **48**, 17780–17791.
64 M. Dolai, M. Ali, C. Rajnák, J. Titiš and R. Boča, *New J. Chem.*, 2019, **43**, 12698–12701.
65 F. Santanni, A. Albino, M. Atzori, D. Ranieri, E. Salvadori, M. Chiesa, A. Lunghi, A. Bencini, L. Sorace, F. Totti and R. Sessoli, *Inorg. Chem.*, 2021, **60**, 140–151.
66 L. Gu and R. Wu, *Phys. Rev. Lett.*, 2020, **125**, 117203.
67 X. Liang, T.-Y. Zhang, X.-Y. Zeng, Y. Zheng, K. Wei and Y.-R. Yang, *J. Am. Chem. Soc.*, 2017, **139**, 3364–3367.
68 G. Huang, B. Kling, F. H. Darras, J. Heilmann and M. Decker, *Eur. J. Med. Chem.*, 2014, **81**, 15–21.
69 Y.-Y. Huang, C. Cai, X. Yang, Z.-C. Lv and U. Schneider, *ACS Catal.*, 2016, **6**, 5747–5763.
70 H. Li, K. M. Belyk, J. Yin, Q. Chen, A. Hyde, Y. Ji, S. Oliver, M. T. Tudge, L.-C. Campeau and K. R. Campos, *J. Am. Chem. Soc.*, 2015, **137**, 13728–13731.
71 G. Li, F. R. Fronczek and J. C. Antilla, *J. Am. Chem. Soc.*, 2008, **130**, 12216–12217.
72 J. Lu, F. Sha and X.-Y. Wu, *Tetrahedron Lett.*, 2019, **60**, 1161–1165.
73 T. Arai, K. Tsuchiya and E. Matsumura, *Org. Lett.*, 2015, **17**, 2416–2419.
74 S. Alvarez, P. Alemany, D. Casanova, J. Cirera, M. Llunell and D. Avnir, *Coord. Chem. Rev.*, 2005, **249**, 1693–1708.
75 D. C. M. Llunell, J. Cirera, P. Alemanyand and S. Alvarez, *Shape v.2.0*, Universitat de Barcelona, 2010.
76 M. Pinsky and D. Avnir, *Inorg. Chem.*, 1998, **37**, 5575–5582.
77 S. Khan, S. Herrero, R. González-Prieto, M. G. B. Drew, S. Banerjee and S. Chattopadhyay, *New J. Chem.*, 2018, **42**, 13512–13519.
78 W. Haase, *Ber. Bunsenges. Phys. Chem.*, 1994, **98**, 1208–1208.
79 N. F. Chilton, R. P. Anderson, L. D. Turner, A. Soncini and K. S. Murray, *J. Comput. Chem.*, 2013, **34**, 1164–1175.
80 D. Aravena and E. Ruiz, *Dalton Trans.*, 2020, **49**, 9916–9928.
81 J. M. Zadrozny, M. Atanasov, A. M. Bryan, C.-Y. Lin, B. D. Rekken, P. P. Power, F. Neese and J. R. Long, *Chem. Sci.*, 2013, **4**, 125–138.
82 K. S. Cole and R. H. Cole, *J. Chem. Phys.*, 1941, **9**, 341–351.
83 Y.-N. Guo, G.-F. Xu, Y. Guo and J. Tang, *Dalton Trans.*, 2011, **40**, 9953–9963.
84 R. Boča, C. Rajnák, J. n. Moncol, J. n. Titiš and D. a. Valigura, *Inorg. Chem.*, 2018, **57**, 14314–14321.
85 K. Fujisawa, A. Tateda, Y. Miyashita, K.-i. Okamoto, F. Paulat, V. K. K. Praneeth, A. Merkle and N. Lehnert, *J. Am. Chem. Soc.*, 2008, **130**, 1205–1213.
86 P. Pietrzyk and Z. Sojka, *J. Phys. Chem. A*, 2005, **109**, 10571–10581.
87 V. Umamaheswari, M. Hartmann and A. Pöppl, *J. Phys. Chem. B*, 2005, **109**, 1537–1546.
88 V. Umamaheswari, M. Hartmann and A. Pöppl, *J. Phys. Chem. B*, 2005, **109**, 10842–10848.
89 F. Aquilante, J. Autschbach, R. K. Carlson, L. F. Chibotaru, M. G. Delcey, L. De Vico, I. F. Galván, N. Ferré, L. M. Frutos, L. Gagliardi, M. Garavelli, A. Giussani, C. E. Hoyer, G. Li Manni, H. Lischka, D. Ma, P. Å. Malmqvist, T. Müller, A. Nenov, M. Olivucci, T. B. Pedersen, D. Peng, F. Plasser, B. Pritchard, M. Reiher, I. Rivalta, I. Schapiro, J. Segarra-Martí, M. Stenrup, D. G. Truhlar, L. Ungur, A. Valentini, S. Vancoillie, V. Veryazov, V. P. Vysotskiy, O. Weingart, F. Zapata and R. Lindh, *J. Comput. Chem.*, 2016, **37**, 506–541.
90 N. M. Atherton, *Principles of electron spin resonance*, Prentice Hall, 1993.
91 H. Husein Mor, H. Weihe and J. Bendix, *J. Magn. Reson.*, 2010, **207**, 283–286.
92 F. Neese, *Wiley Interdiscip. Rev.: Comput. Mol. Sci.*, 2012, **2**, 73–78.
93 S. K. Misra, *Multifrequency Electron Paramagnetic Resonance*, erratum, ed. S. K. Misra and C. Rudowicz, Wiley-VCH, Weinheim, 2011, **https://www.wiley-vch.de/publish/dt/books/ISBN3-527-40779-0/**.
94 P. P. M. Valko, S. Biskupič and M. Mazúr, *Chem. Pap.*, 1990, **44**, 805–813.
95 A. Drzewiecki, B. Padlyak, V. Adamiv, Y. Burak and I. Teslyuk, *Nukleonika*, 2013, **58**, 379–385.
96 J. L. Rao, G. Sivaramaiah and N. Gopal, *Phys. B*, 2004, **349**, 206–213.
97 R. Ravikumar, R. Komatsu, K. Ikeda, A. Chandrasekhar, B. Reddy, Y. Reddy and P. S. Rao, *J. Phys. Chem. Solids*, 2003, **64**, 261–264.
98 A. Abragam and B. Bleaney, *Electron Paramagnetic Resonance of Transition Ion*, Clarendon Press, Oxford, 1970.
99 E. Garribba and G. Micera, *J. Chem. Educ.*, 2006, **83**, 1229.
100 Z. Wen-Chen and W. Shao-Yi, *Z. Naturforsch.*, 2000, **55**, 915–917.
101 M.-Q. Kuang, L.-D. Wang and S.-K. Duan, *J. Phys. Chem. Solids*, 2017, **111**, 41–46.

102 H.-M. Zhang and X. Wan, *J. Non-Cryst. Solids*, 2013, **361**, 43–46.
103 S.-Y. Wu, H.-M. Zhang, P. Xu and S.-X. Zhang, *Spectrochim. Acta, Part A*, 2010, **75**, 230–234.
104 M.-Q. Kuang, S.-Y. Wu, G.-L. Li and X.-F. Hu, *Mol. Phys.*, 2015, **113**, 698–702.
105 S. Y. WU, J. S. YAO, H. M. ZHANG and G. D. LU, *Int. J. Mod. Phys. B*, 2007, **21**, 3250–3253.
106 K. Min-Quan, W. Shao-Yi, H. Xian-Fen and S. Bo-Tao, *Z. Naturforsch., A: Phys. Sci.*, 2013, **68**, 442–446.
107 L. Chao-Ying, H. Ying and Z. Xue-Mei, *Phys. B*, 2015, **456**, 125–128.
108 M.-Q. Kuang, S.-Y. Wu and H.-M. Zhang, *Optik*, 2012, **123**, 1601–1604.
109 M.-Q. Kuang, S.-Y. Wu, X.-F. Hu and B.-T. Song, *Phys. B*, 2013, **417**, 13–16.
110 D. J. Newman and B. Ng, *Rep. Prog. Phys.*, 1989, **52**, 699–762.
111 C. A. Morrison, in *Crystal Fields for Transition-Metal Ions in Laser Host Materials*, ed. C. A. Morrison, Springer Berlin Heidelberg, Berlin, Heidelberg, 1992, pp. 1–2. DOI: **10.1007/978-3-642-95686-7_1**.
112 B. G. Wybourne, *Spectroscopic Properties of Rare Earths*, Interscience Publishers, 1965.
113 C. Rudowicz, in *Computer package CST: conversions, standardization and transformations*, ed. B. Ng and D. J. Newman, Cambridge University Press, Cambridge, 2000, p. 259.
114 C. Rudowicz and Q. Jian, *Comput. Chem.*, 2002, **26**, 149–157.
115 C. Rudowicz and R. Bramley, *J. Chem. Phys.*, 1985, **83**, 5192–5197.
116 C. Rudowicz and P. Gnutek, *Phys. B*, 2010, **405**, 113–132.
117 J. S. Griffith, *The theory of transition-metal ions*, Cambridge University Press, 1964.
118 Y. Y. Yeung and C. Rudowicz, *Comput. Chem.*, 1992, **16**, 207–216.
119 G. W. Burdick and M. F. Reid, *Mol. Phys.*, 2004, **102**, 1141–1147.
120 M. Karbowiak, C. Rudowicz and P. Gnutek, *Opt. Mater.*, 2011, **33**, 1147–1161.
121 M. Karbowiak, P. Gnutek and C. Rudowicz, *Chem. Phys.*, 2012, **400**, 29–38.
122 M. A. Halcrow, *Chem. Soc. Rev.*, 2013, **42**, 1784–1795.
123 J. Miklovič, D. Valigura, R. Boča and J. Titiš, *Dalton Trans.*, 2015, **44**, 12484–12487.
124 M. Briganti, F. Santanni, L. Tesi, F. Totti, R. Sessoli and A. Lunghi, *J. Am. Chem. Soc.*, 2021, **143**, 13633–13645.